minerals

MDPI

Article

Geochemical Features of Redox-Sensitive Trace Metals in Sediments under Oxygen-Depleted Marine Environments

Moei Yano [1,2], Kazutaka Yasukawa [1,2,3], Kentaro Nakamura [3], Minoru Ikehara [4] and Yasuhiro Kato [1,2,3,5,*]

[1] Ocean Resources Research Center for Next Generation, Chiba Institute of Technology, 2-17-1 Tsudanuma, Narashino, Chiba 275-0016, Japan; moei.yano@p.chibakoudai.jp (M.Y.); k-yasukawa@sys.t.u-tokyo.ac.jp (K.Y.)
[2] Frontier Research Center for Energy and Resources, School of Engineering, The University of Tokyo, 7-3-1 Hongo, Bunkyo-ku, Tokyo 113-8656, Japan
[3] Department of Systems Innovation, School of Engineering, The University of Tokyo, 7-3-1 Hongo, Bunkyo-ku, Tokyo 113-8656, Japan; kentaron@sys.t.u-tokyo.ac.jp
[4] Center for Advanced Marine Core Research, Kochi University, B200 Monobe, Nankoku, Kochi 783-8502, Japan; ikehara@kochi-u.ac.jp
[5] Submarine Resources Research Center, Research Institute for Marine Resources Utilization, Japan Agency for Marine-Earth Science and Technology, 2-15 Natsushima-cho, Yokosuka, Kanagawa 237-0061, Japan
* Correspondence: ykato@sys.t.u-tokyo.ac.jp; Tel.: +81-3-5841-7022

Received: 13 September 2020; Accepted: 13 November 2020; Published: 17 November 2020

Abstract: Organic- and sulfide-rich sediments have formed in oxygen-depleted environments throughout Earth's history. The fact that they are generally enriched in redox-sensitive elements reflects the sedimentary environment at the time of deposition. Although the modern ocean is well oxidized, oxygen depletion occurs in certain areas such as restricted basins and high-productivity zones. We measured bulk chemical compositions (major and trace elements, total organic carbon, and total sulfur) of organic- and sulfide-rich sediments collected from eight areas having oxygen-depleted water to discuss relationships between geochemical features and sedimentary environments. Major elemental compositions generally show mixtures of terrigenous detritus and biogenic carbonate. Some redox-sensitive elements might be controlled by organic matter content, whereas others could be contained in sulfide minerals in sediments. In particular, Mo and U show a characteristic trend; areas with higher Mo and U—at least partially owing to a depositional process called the "particulate shuttle"—generally correspond to regions influenced by the open ocean. In contrast, areas with lower Mo and U are more restricted marine environments. This suggests that the degree of Mo and U enrichment reflects the geography in terms of proximity to the open ocean, or the degree of the supply of these elements from the open ocean.

Keywords: sediment geochemistry; oxygen-depleted conditions; redox-sensitive elements; organic-rich sediment; Deep Sea Drilling Project; Ocean Drilling Program; International Ocean Discovery Program

1. Introduction

Organic-rich and laminated sediments are formed under oxygen-depleted conditions where the decomposition of organic matter and activity of benthic organisms decrease. In particular, the lithified form of these deposits is called "black shale". As a record of a reducing marine environment, several redox-sensitive and sulfide-forming trace elements such as As, Cu, Mo, Ni, Re, U, V and Zn are concentrated in black shale by adsorbing on organic matter or forming sulfides [1–5]. Many researchers have reconstructed paleoceanographic conditions and their short- and long-term changes from the geochemical features of these elements in black shale formed in the geologic past [6–17].

For Devonian–Mississippian black shale in central Kentucky (USA), it has been proposed that the Sunbury Shale (Tournasian, Lower Mississippian) was deposited under anoxic (possibly even euxinic) conditions, whereas the Ohio New Albany Shale (Fammenian, Upper Devonian) may have accumulated under a relatively wide range of redox conditions, on the basis of redox-sensitive elements (especially Mo, V) and trace-element redox indices (especially Ni/Co, V/Cr and V/[V + Ni]) [6,7]. On the other hand, the modeling of the marine Mo inventory suggests trace element drawdown in late Devonian seawater [8]. For the Permian–Triassic boundary (PTB), iron speciation and authigenic concentrations and enrichment factors of Mo, V, and U in the Meishan-1 core near the Global Stratotype Section and Point (GSSP) suggest that the interval corresponding to the end-Permian marine extinction was deposited under a persistently anoxic water mass with intermittently euxinic bottom water [9]. Regarding the Early Triassic, Grasby et al. [10] concluded that recurrent anoxic to euxinic conditions developed at Sverdrup Basin near northwest Pangea, on the basis of Mo:Al ratios and pyrite contents.

There have also been extensive discussions concerning redox conditions in pelagic Panthalassa across the PTB. Reducing bottom water conditions are indicated on the basis of a Ce anomaly change and Mn depletion [11], Mo, V, U and Cr concentrations [12], and chemical species of Fe and Mo [13]. However, Algeo et al. [14] suggested spatially heterogeneous redox conditions in the Panthalassa at the PTB: intensified anoxia or euxinia in the oxygen-minimum zone in the upper water column and oxic to suboxic bottom water. In addition to the oceanic redox conditions, significant depletion of bioessential elements in seawater has been proposed; for example, Cr, V, and Mo [9,12] as well as U [15]. For the Cretaceous Ocean Anoxic Event (OAE) 1a, Westermann et al. [16] looked at redox sensitive elements (e.g., Mo and U), total organic carbon (TOC), and phosphorus accumulation rates, and they suggested that productivity may have played a key role in the widespread development of the anoxic conditions in the western Tethys Ocean. Moreover, redox-sensitive elements have been used to estimate depositional environments, such as the expansion of the oxygen minimum zone at the Demerara Rise in the tropical Atlantic Ocean during OAE2 [17].

In contrast to these environmental upheavals in the geologic past, the modern ocean is dominated by oxidative conditions from the surface to the deep, owing to a vigorous overturning circulation (e.g., [18]). In the modern ocean, therefore, oxidative sediments such as pelagic clay prevail worldwide. They in turn concentrate other types of elements that are precipitated and preserved in Ca-phosphates or Fe-Mn oxides under oxic conditions (e.g., rare-earth elements (REE), Mn, or Co; [19–25]). Because such oxidative conditions in the deep ocean have been maintained since the late Cretaceous [26], some types of pelagic clay that have accumulated very slowly are reported to contain remarkably high concentrations of REE [27–31] and characterize the sediments deposited in the modern deep-sea basins as an integration of the oceanic environmental record for tens of millions of years [22,32–36].

Even in the predominantly oxic modern ocean, however, anoxic water masses develop in a few types of sea areas, such as restricted basins and high-productivity zones. For example, the Black Sea [37], Cariaco Basin [38], Saanich Inlet [39] and Framvaren Fjord [40] reportedly have blackish, organic- and/or sulfide-rich sediments, which reflects the development of oxygen-depleted conditions in the deeper part of the water column. These sediments should have characteristic chemical compositions reflecting their depositional environments (e.g., variations in redox conditions of water/sediment columns, geographical conditions, or differences in lithofacies of hinterlands). Clarifying the geochemical features of modern sediments, including some of the redox-sensitive elements, can provide new insights into paleoenvironmental conditions under which the ancient counterparts of the modern organic- and sulfide-rich sediments were deposited. From this perspective, several researchers have investigated the geochemistry of such modern organic- and sulfide-rich sediments that were deposited under various anoxic environments [41–43]. Algeo and Tribovillard (2009) [42] systematically characterized Mo–U covariations from various modern sea areas and successfully applied these geochemical tracers to Paleozoic black shales.

In this study, we analyzed the chemical composition of the sediments from eight different geographical settings, namely the Red Sea, Black Sea, Gulf of California, Cariaco Basin, Saanich Inlet, Namibian Shelf, Bight of Angola and Baltic Sea. These are known as regions containing blackish sediments that are potentially enriched in organic matter and/or sulfide minerals being deposited and preserved under oxygen-depleted conditions. Based on our analytical results, including the behaviors of redox-sensitive elements, we discuss the relationships between their geochemical features and their depositional environments.

2. Materials and Methods

2.1. Geological Settings and Samples

We used sediment samples collected at the seafloor under oxygen-depleted conditions by the Deep Sea Drilling Project (DSDP), Ocean Drilling Program (ODP) and International Ocean Discovery Program (IODP). We analyzed 163 samples in total, taken from 12 sites in eight sea areas (Figure 1).

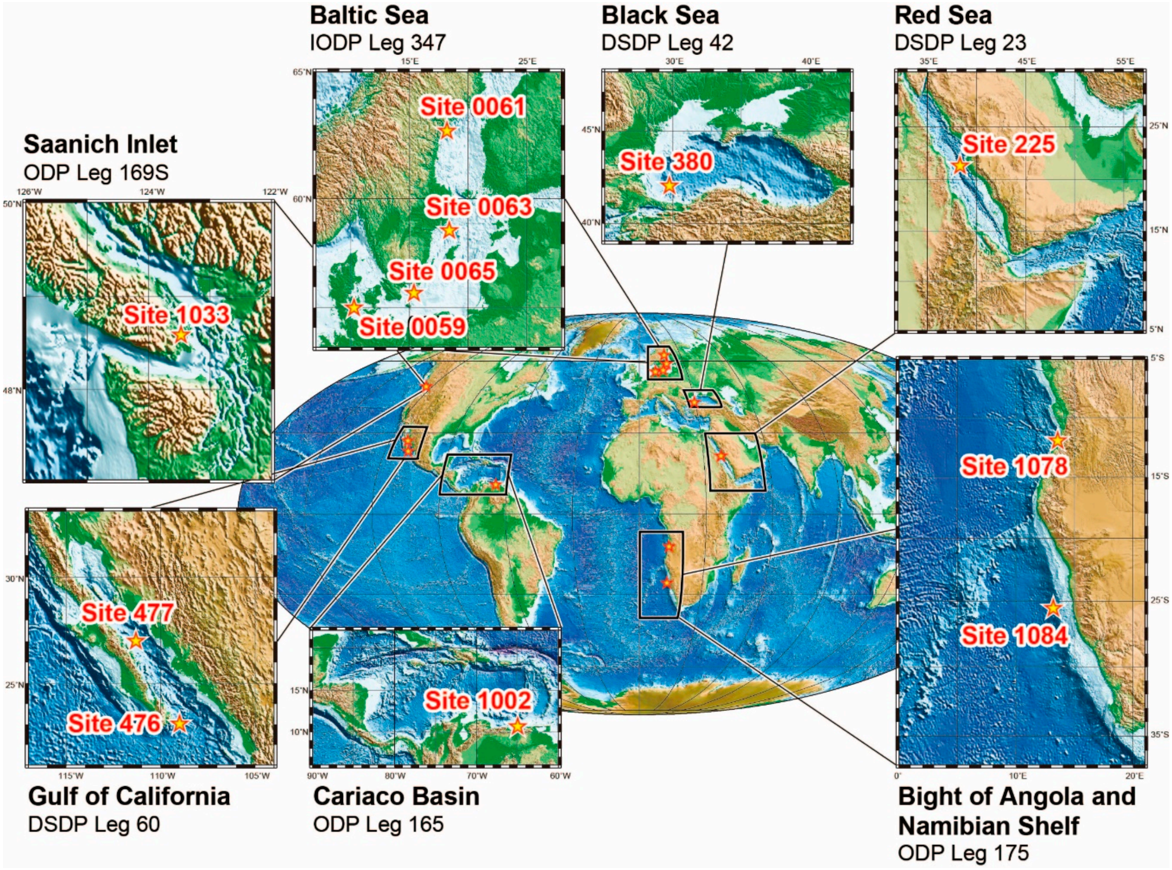

Figure 1. Locations of the Deep Sea Drilling Project (DSDP)/Ocean Drilling Program (ODP)/International Ocean Discovery Program (IODP) sites that were sources of sediments analyzed in this study.

DSDP Site 225 is at 21°18.58′ N, 38°15.11′ E and 1228 m water depth, on the eastern edge of the axial trough of the Red Sea. This site was drilled to a depth of 230 m below the seafloor (mbsf). We analyzed 15 samples between the core top and 194.39 m (Lithological Units I to IV; [44]). Unit I, from core top to 112 mbsf, consists of foraminifer-bearing, micarb-rich, clayey-silt nanno-ooze and chalk [44] (Figure 2). The sediments show a variety of colors (light to dark gray) and are interpreted to reflect the Eh of the sediment surface at the time of their deposition [44]. The dark layers are enriched in organic matter and pyrite [44]. Unit II (from 112 to 167 mbsf) is characterized by micarb- and nanno-rich silty claystone [44]. There are alternating light-gray and dark-gray layers, similar to Unit I. The dark-gray layers are enriched in organic matter and pyrite [44]. Unit III (from 167 to 176 mbsf) consists of dolomitic silty claystone [44]. Sediment colors are dark gray to black, and some parts show a slight lamination. Unit IV (from 176 to 230 mbsf) is characterized by anhydrite and halite [44]. Several laminated black-shale layers that are composed of clay, organic matter, and pyrite are contained in the evaporite facies.

DSDP Site 380 is at 42°05.94′ N, 29°36.82′ E and 2107 m water depth, near the Bosporus Strait, southwest of the Black Sea. Total penetration of the drilling was 1073.5 m. We analyzed 45 samples between 971.76 and 1074.8 mbsf (Lithological Unit V; [45]). Unit V consists of black shales with zeolitic sandstones and dolomite [45] (Figure 2). The black shales are greenish black in color, fissile, and consist of clay and organic matter [45]. The presence of a small benthic foraminifer suggests that the black shales and associated sediments were deposited in a brackish–marine environment [45].

DSDP Site 476 is at 23°02.43′ N, 109°05.35′ W and 2403 m water depth, on the continental slope about 40 km southeast of the tip of the Baja California Peninsula. This site was drilled to a depth of 294.5 m. We analyzed 10 samples between the seafloor and 14.25 mbsf (Lithological Unit I; [46]). From core top to 66 mbsf, Unit I comprises mostly nannofossil ooze, nannofossil–diatom ooze, and diatomaceous ooze to nannofossil–diatom-bearing mud [46] (Figure 2). Colors of the sediments vary among grayish olive green, light olive, grayish olive, and dusky yellow green or moderate olive brown [46].

DSDP Site 477 is at 27°01.85′ N, 111°24.02′ W and 2003 m water depth, in the southern rift of the Guaymas Basin, Gulf of California. We used samples from Hole 477, whose total penetration was 191.0 m. We analyzed five samples between the seafloor and 12.55 mbsf (Lithological Unit I; [46]). From the seafloor to 58 mbsf, sediments are moderate-olive-brown to grayish-olive diatomaceous oozes and silty sands and appear quite uniform in texture [46] (Figure 2).

ODP Site 1002 is at 10°42.368′ N, 65°10.161′ W and 893.6 m water depth, on the central saddle of the Cariaco Basin on the northern continental shelf of Venezuela. We used samples from Hole 1002D, which was cored from the sediment surface to 166.8 mbsf. We analyzed 20 samples between the seafloor and 44.95 mbsf (Lithological Unit I, Subunits IA–ID; [47]). From the seafloor to 5.5 mbsf, Subunit IA consists of dark olive-gray silty clay with nannofossils and foraminifers [47] (Figure 2). From 5.5 to 7.4 mbsf, Subunit IB consists of a colorful mixture of fine-grained clay [47]. From 7.4 to 43.79 mbsf, Subunit IC consists of olive-gray to light olive-gray laminated nannofossil silty clay [47]. From 43.79 to 45.20 mbsf, Subunit ID is olive-gray nannofossil silty clay [47].

ODP Site 1033 is at 48°35.434′ N, 123°30.200′ W and 226.5 m water depth, in Saanich Inlet, a fjord on southeastern Vancouver Island, 25 km north of Victoria, British Columbia (Canada). We used samples from Hole 1033D, whose total penetration was 69.7 m. We analyzed 18 samples between the seafloor and 52.95 mbsf (Lithological Units I and II; [48]). From the seafloor to 46.66 mbsf, Unit I comprises olive-gray and gray diatomaceous muds [48] (Figure 2). From 46.66 m to 69.7 m, Unit II is predominantly composed of rapidly accumulated dense, massive gray to olive-gray terrigenous silty clay [48].

ODP Site 1078 is at 11°55.2145′ S, 13°24.0134′ E and 427.2 m water depth, outside the Bight of Angola. We used samples from Hole 1078A, whose total penetration was 77.1 m. We analyzed 10 samples between the seafloor and 38.82 mbsf. Sediment is composed predominantly of a moderately bioturbated, olive-gray and dark olive-gray silty clay with varying amounts of nannofossils and foraminifers [49] (Figure 2).

ODP Site 1084 is at 25°30.8345′ S, 13°1.6668′ E and 1991.9 m water depth, in Lüderitz Bay, Namibia, and close to the major upwelling centers along southwest Africa. We used samples from Hole 1084A, which was drilled to a depth of 605 mbsf. We analyzed 10 samples between the seafloor and 36.64 mbsf (Lithological Unit I, Subunit IA; [49]). Subunit IA is composed of moderately bioturbated olive-gray, very dark grayish-brown, and olive foraminifer- and diatom-bearing nannofossil clay, and foraminifer-bearing diatom-rich clayey nannofossil ooze [49] (Figure 2).

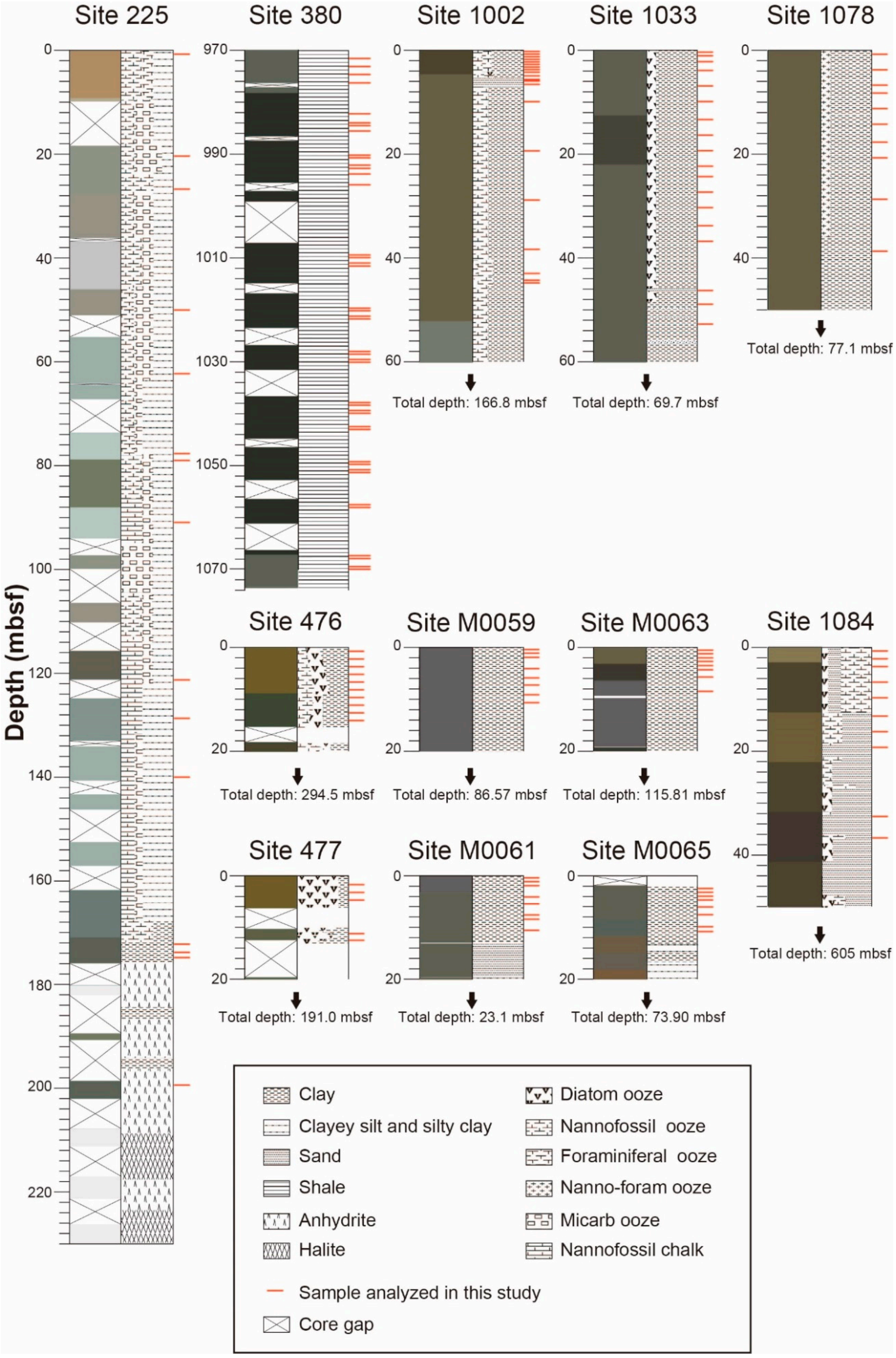

Figure 2. Lithostratigraphy of the analyzed sites. Sources of lithostratigraphic information are as follows: Site 225 [44]; Site 380 [45]; Sites 476 and 477 [46]; Site 1002 [47]; Site 1033 [48]; Sites 1078 and 1084 [49]; Sites M0059, M0061, M0063 and M0065 [50]. mbsf, meters below sea floor.

IODP Site M0059 is at 55°0.29′ N, 10°6.49′ E and 35 m water depth, in the southern Little Belt, southern Denmark. We used samples from Hole M0059D, which was drilled to a depth of 86.57 m. We analyzed eight samples between the seafloor and 10.67 mbsf (Lithological Unit I, Subunit Ia; [50]). From the seafloor to 50.06 mbsf, sediment is composed of black to greenish-black well-sorted clay [50] (Figure 2).

IODP Site M0061 is at 62°46.70′ N, 18°02.95′ E and 86 m water depth, near the mouth of the Ångermanälven River estuary, eastern Sweden. We used samples from Hole M0061C drilled to a depth of 23.1 mbsf. We analyzed eight samples between the seafloor and 10.67 mbsf (Lithological Units I–III; [50]). From the seafloor to 2.44 mbsf (Unit I), the sediment is mainly composed of a greenish-gray to black clay [50] (Figure 2). From 2.44 to 8.74 mbsf, Unit II consists of dark greenish-gray silty-sandy organic-rich clay [50]. From 8.74 to 15.20 mbsf, Unit III is dark greenish-gray interlaminated clayey silt and silt [50].

IODP Site M0063 is at 58°37.34′ N, 18°15.25′ E and 451 m water depth, in the central part of the Landsort Deep, southeast of Sweden. We used samples from Hole M0063A drilled to a depth of 115.81 mbsf. We analyzed eight samples from the seafloor to 8.50 mbsf (Lithological Unit I, Subunits Ia–Ic; [50]). From the seafloor to 3.54 mbsf, Subunit Ia consists of very-well-sorted black organic-rich clay [50] (Figure 2). No primary sedimentary structures were visible because of the high degree of gas expansion [50]. From 3.54 to 7.89 mbsf, Subunit Ib consists of black clay. From 7.89 to 19.92 mbsf, Subunit Ic is very-well-sorted black organic-rich clay [50].

IODP Site M0065 is at 55°43.27′ N, 15°13.59′ E and 87 m water depth, northeast of the island of Bornholm, between Sweden and Poland. We used samples from Hole M0065A drilled to a depth of 73.90 mbsf. We analyzed eight samples from the seafloor to 10.80 mbsf (Lithological Units I and II; [50]). From the seafloor to 9.18 mbsf (Unit I), the sediment consists of very-well-sorted dark greenish-gray organic-rich clay [50] (Figure 2). From 9.18 to 13.85 mbsf (Unit II), the clay is gray to dark gray [50].

2.2. Sample Processing and Analytical Methods

Sediment samples were dried at 40 °C and ground to powder with an agate mortar and pestle. Before each analysis described below, the powdered samples were further dried at 110 °C for ~12 h to remove adsorbed water. Loss on ignition (LOI) was determined on the basis of weight loss during combustion at 950 °C for over 6 h. Major element contents were measured using an X-ray fluorescence (XRF) spectrometer (Rigaku ZSX Primus II) at the Department of Systems Innovation, The University of Tokyo. Analytical procedures follow those described by Kato et al. [11,51,52] and Yasukawa et al. [20]. The XRF analysis was conducted on glass beads made using 0.4 g of the combusted sample powder mixed well with 4.0 g of $Li_2B_4O_7$ flux and fused at 1190 °C for 7 min in a Pt crucible. Multiple geochemical reference materials issued by the Geological Survey of Japan, including igneous rock standards (JB-1b: basalt, JB-2: basalt, JG-2: granite, JR-1: rhyolite, JA-1: andesite, etc.) and sediment/sedimentary rock standards (JDo-1: dolomite, JSd-3: river sediment, JSl-2: slate, etc.), were used as calibration standards. The XRF analytical method is modified from Irino [53].

Trace-element abundances were determined using an inductively coupled plasma quadrupole mass spectrometer (ICP-QMS) (iCAP Q, Thermo Fisher Scientific) installed at the Department of Systems Innovation, The University of Tokyo. The analytical procedures were based on those described by Kato et al. [11,51,52] and Yasukawa et al. [20,35]. For analysis, 0.05 g of sample powder was dissolved in HNO_3–HF–$HClO_4$ (2 mL, 4 mL, and 0.8 mL, respectively) in tightly sealed, 10-mL perfluoroalkoxy alkane (PFA) screw-cap beakers and heated for 2 h on a hot plate set at 130 °C. The dissolved samples were progressively evaporated at 110 °C for 12 h, at 160 °C for 6 h, and at 190 °C until dry. The residues were then dissolved in 4 mL of aqua regia on a hot plate at 90 °C for 6 h. The digested samples were progressively evaporated at 120 °C for 2 h, then at 160 °C until dry. The residues were then dissolved in 10 mL of 2 wt% of mixed acid of HNO_3:HCl:HF = 20:5:1 on a hot plate at 90 °C for 3 h. The solution was diluted to 1:10,000 by mass using the same 2 wt% HNO_3–HCl–HF mixed acid. Spectral overlaps from oxides and hydroxides ($^{44}Ca^{16}O$ on ^{60}Ni, $^{47}Ti^{16}O$ on ^{63}Cu, $^{50}Ti^{16}O$ on ^{66}Zn, $^{13}7Ba^{16}O$ on ^{153}Eu,

$^{141}Pr^{16}O$ and $^{140}Ce^{16}O^{1}H$ on ^{157}Gd, $^{143}Nd^{16}O$ on ^{159}Tb, $^{147}Sm^{16}O$ and $^{146}Nd^{16}O^{1}H$ on ^{163}Dy, $^{149}Sm^{16}O$ on ^{165}Ho, $^{150}Nd^{16}O$ and $^{150}Sm^{16}O$ on ^{166}Er, and $^{165}Ho^{16}O$ on ^{181}Ta) were corrected following the method described by Aries et al. [54]. Analyses were generally within 5% (relative percent difference) of the accepted values of reference materials JB-2, JB-3 [55] and JMS-2 [56] issued by the Geological Survey of Japan.

Prior to total organic carbon (TOC) analysis, inorganic carbonate was removed following procedures described by Larson et al. [57]. For this removal, 100–300 mg of samples were put into centrifuge tubes and treated with 10 mL of 6 N HCl at 60 °C for 72 h. Samples were then washed in Milli-Q water to a neutral pH and dried at 60 °C for >24 h. Before the analysis, samples were further dried at 110 °C for 12 h to remove adsorbed water and weighed into tin foil cups. Analyses were conducted using a CHNS/O elemental analyzer (Flash EA1112, Thermo Fisher Scientific) at the Center for Advanced Marine Core Research, Kochi University. Sulfanilamide was used as a calibration standard. The TOC content for bulk samples was calculated using the TOC content of the decarbonated sample and the total carbon (TC) content from the untreated sample. Total sulfur (TS) analyses were conducted in the same manner as TOC using untreated samples.

To measure the degree of elemental enrichment, we calculated "enrichment factors" (EFs) relative to the average upper continental crust (UCC; Rudnick and Gao, [58]) as follows:

$$X_{EF} = [(X/Al)_{sample}/(X/Al)_{UCC}], \tag{1}$$

where X and Al stand for the weight concentrations of elements X and Al, respectively.

3. Results and Discussion

3.1. Geochemical Features of the Sediments Suggested by Major Elements

All of the analytical results are presented in Supplementary Table S1. Overall, the samples show positive correlations for SiO_2, TiO_2, K_2O, and Fe_2O_3 vs Al_2O_3 (Figure 3a–d). The data distributions show linear trends as a whole toward the compositional range of terrigenous detrital materials potentially relating to the studied samples, including Svecofennian granite, central Sweden [59] for Baltic Sea, Cariaco Shelf sediment of terrigenous origin [60] for Cariaco Basin, North American shale composite (NASC) [61] for Gulf of California and Saanich Inlet, and the average UCC. This indicates that the sediments having relatively high Al_2O_3, SiO_2, TiO_2, and K_2O contents mainly comprise detrital materials. Because SiO_2:Al_2O_3 ratios of almost all of the samples fall within those of the reference terrigenous materials described above (Figure 3a), the studied sediments are not greatly affected by biogenic silica, which can cause positive SiO_2:Al_2O_3 deviations. On the other hand, the samples overall show negative correlations in SiO_2, TiO_2, K_2O, and Fe_2O_3 vs CaO (Figure 3e–h). These trends suggest that these elemental contents are diluted by CaO. In the samples from the Cariaco Basin and Namibian Shelf (Site 1084) that have high CaO contents (up to ~42 wt%), foraminifers were identified before the pulverization. Therefore, these negative correlations reflect a mixture of terrigenous detrital materials and biogenic carbonate. Baltic Sea samples which have high potassium contents might be affected by terrigenous materials from Svecofennian granite (Figure 3c,e). As a whole, the fundamental structure of the major element composition of the studied samples is controlled by the mixture of various terrigenous detrital materials and biogenic carbonate.

In the Al_2O_3–Fe_2O_3 and CaO–Fe_2O_3 diagrams (Figure 3d,h), a subset of the samples from the Red Sea deviates from the major linear trends described above and shows Fe-enrichment. These are probably affected by hydrothermal activity. The MnO contents of the samples, except for the highest values in three samples from the Baltic Sea (Site M0063), show no more than ~0.4%, and almost all of the samples have ~0.1% MnO. The very low MnO contents suggest that the sediments in this study were affected by oxygen-depleted conditions where Mn oxides cannot exist stably. For the samples having high MnO contents, diagenetic processes might have altered the primary signals after deposition.

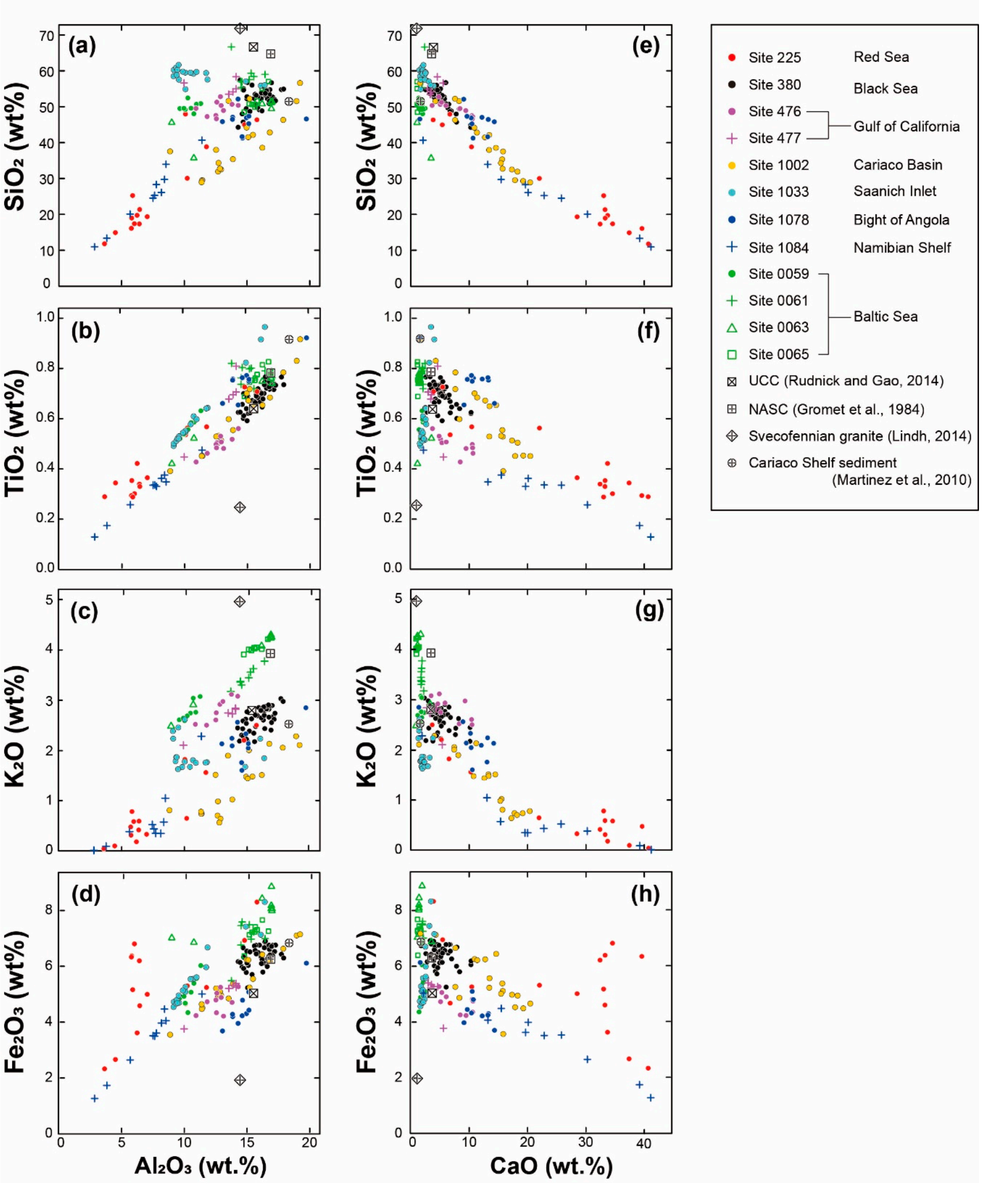

Figure 3. Scatter-diagrams of elemental contents in bulk sediments: relationships between Al_2O_3 and (**a**) SiO_2, (**b**) TiO_2, (**c**) K_2O and (**d**) Fe_2O_3, and between CaO and (**e**) SiO_2, (**f**) TiO_2, (**g**) K_2O and (**h**) Fe_2O_3. UCC, upper continental crust [58], NASC, North American shale composite [61], Svecofennian granite, central Sweden [59] and Cariaco Shelf sediment [60].

3.2. Relationships between Concentrations of Trace Elements, Total Organic Carbon, and Total Sulfur

Although the TOC data analyzed in this study are generally consistent with literature values (e.g., 0.5–2.5% for Site 1033 [48], 1.1–4.1% for Site 1078 [49] and 0.5–2.1% for Site M0061 [50]), the TOC data for two sites (Sites 225 and 1084) show large differences from comparable ones in previous reports (i.e., from similar depths and the same lithological units). This is probably because our HCl treatment could have dissolved excess acid-reactive materials other than carbonates in these samples. Thus, the TOC data for Sites 225 and 1084 are not included in the following discussion.

Covariations of TOC contents and elemental enrichment factors show different trends depending on the elements. TOC vs. U_{EF} (Figure 4a) shows a positive correlation overall for the samples. Although other elemental enrichment factors do not exhibit clearly linear relationships as a whole, several TOC vs. X_{EF} diagrams depict characteristics for each sea area (Figure 4b,c). For TOC vs. Cu_{EF} (Figure 4b), whereas the Cariaco Basin sediments (Site 1002; yellow circles) show that Cu_{EF} is less variable against changes in TOC contents (r = 0.36), the Black Sea Unit V sediments (Site 380; black circles) show a positive correlation (r = 0.75). On the other hand, for TOC vs. Ni_{EF} (Figure 4c), the Cariaco Basin sediments exhibit a positive correlation (r = 0.88), whereas Ni_{EF} of the Black Sea Unit V sediments has a more ambiguous relationship with TOC contents (r = 0.48). These variations among the sea areas can be attributed to differences in environmental factors such as types of organic matter, redox conditions of seawater, and amounts of trace-metals in seawater.

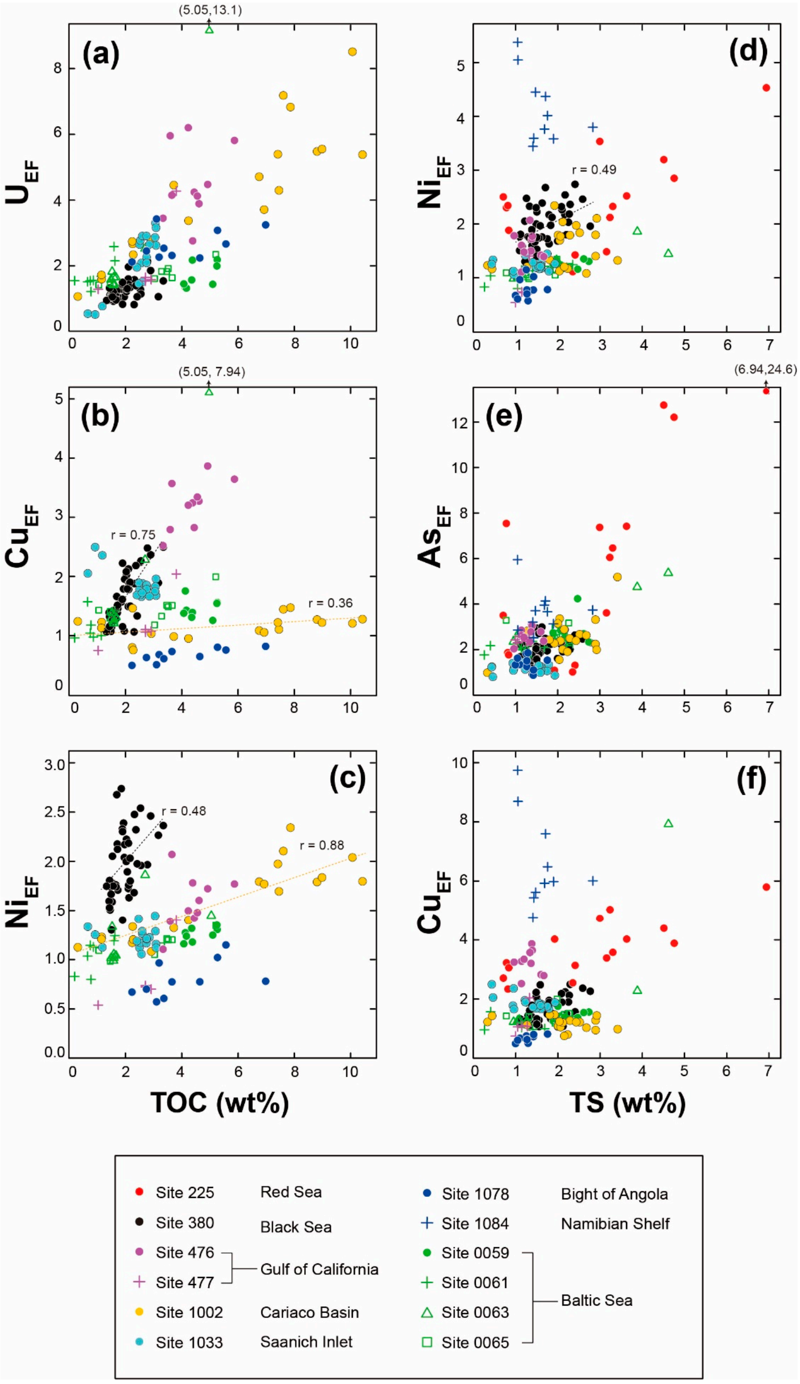

Figure 4. Scatter-diagrams of total organic carbon (TOC) and total sulfur (TS) contents versus enrichment factors for representative redox-sensitive or sulfide-forming elements: TOC versus (**a**) U_{EF}, (**b**) Cu_{EF} and (**c**) Ni_{EF}, and TS versus (**d**) Ni_{EF}, (**e**) As_{EF} and (**f**) Cu_{EF}. Enrichment factors were calculated relative to the average upper continental crust (UCC, see text). Dotted lines in (**a**), (**b**), and (**d**) show regression lines for Sites 380 and 1002 that are mentioned in the text.

As with the TOC–Ni_{EF} covariation, the Ni_{EF} of Black Sea Unit V sediments (Site 380; black circles) also shows a weakly positive correlation with TS contents (r = 0.49) (Figure 4d). This suggests that the moderate Ni enrichment in the Black Sea could be involved with both organic matter and sulfide minerals somewhat randomly or independently; for instance, dissolved Ni could be adsorbed on settling organic matter and/or incorporated into authigenic pyrite in the anoxic water column. On the other hand, for both TS vs. As_{EF} and TS vs Cu_{EF} (Figure 4e,f), the positive correlations shown by the Red Sea sediments (Site 225; red circles) indicate that concentrations of these elements are controlled by sulfides. In contrast, the Cu_{EF} of the Namibian shelf sediment (Site 1084; blue crosses) is unrelated to TS (Figure 4f).

3.3. Characteristics of Enrichment Factors for Redox Sensitive Elements

We prepared scatter diagrams of all pairs of enrichment factors for V, Cr, Co, Ni, Cu, Zn, As, Mo and U (Supplementary Figure S1). Although there is large variation in the data distribution for each pair of elements, these elements generally show weakly to strongly positive correlations (r = 0.24 to 0.84; Supplementary Figure S1) with $p < 0.005$ for a test of no correlation, suggesting that their correlations seem to be statistically significant. This suggests that these redox-sensitive elements commonly accumulate under oxygen-depleted conditions as expected. It should be noted, however, that Cr alone does not show any clear relationship (r > 0.75) with other elements except for Ni. From this we infer that the enrichment of Cr in marine sediments is controlled by materials or processes different than other redox-sensitive elements. In the Cr_{EF}–Ni_{EF} diagram, the Namibian shelf samples (Site 1084) show higher Cr and Ni enrichment than those in other sites. The Namib Desert near this site is relatively rich in heavy minerals such as pyroxene which was transported by the Orange River and shows high Cr content (without Ni enrichment) [62]. The influence of this terrigenous detrital component may enhance the Cr_{EF} of the bulk sediment of this site and increase the correlation coefficient of Cr_{EF}–Ni_{EF} in combination with the high Ni_{EF} at this site (see below).

In the Ni_{EF}–Cu_{EF} covariation (Figure 5), rather than being randomly dispersed, the samples form clusters by each sea area. Under oxygen-depleted conditions in the presence of sufficient sulfide ions, both Ni and Cu precipitate as independent sulfide mineral phases or are taken up by Fe-sulfides (e.g., pyrite) as a solid solution, although they have different speeds of reaction kinetics compared with Fe^{2+} [63,64]. Thus, the linear relationship between Ni_{EF} and Cu_{EF} may indicate that their geochemical behavior under anoxic conditions is mainly controlled by sulfide mineral precipitation [2,4]. On the other hand, the clustering of each sea area implies that there are also other factors affecting the sediment geochemistry. Because Ni and Cu are used for palaeoproductivity markers (e.g., Soua [65]), primary productivity is likely to be an important factor. If this is the case, then the fact that the highest enrichment factors for Ni and Cu are in Namibian shelf sediments (Site 1084; blue crosses) could indicate high productivity owing to the vigorous upwelling of nutrient-rich water [66].

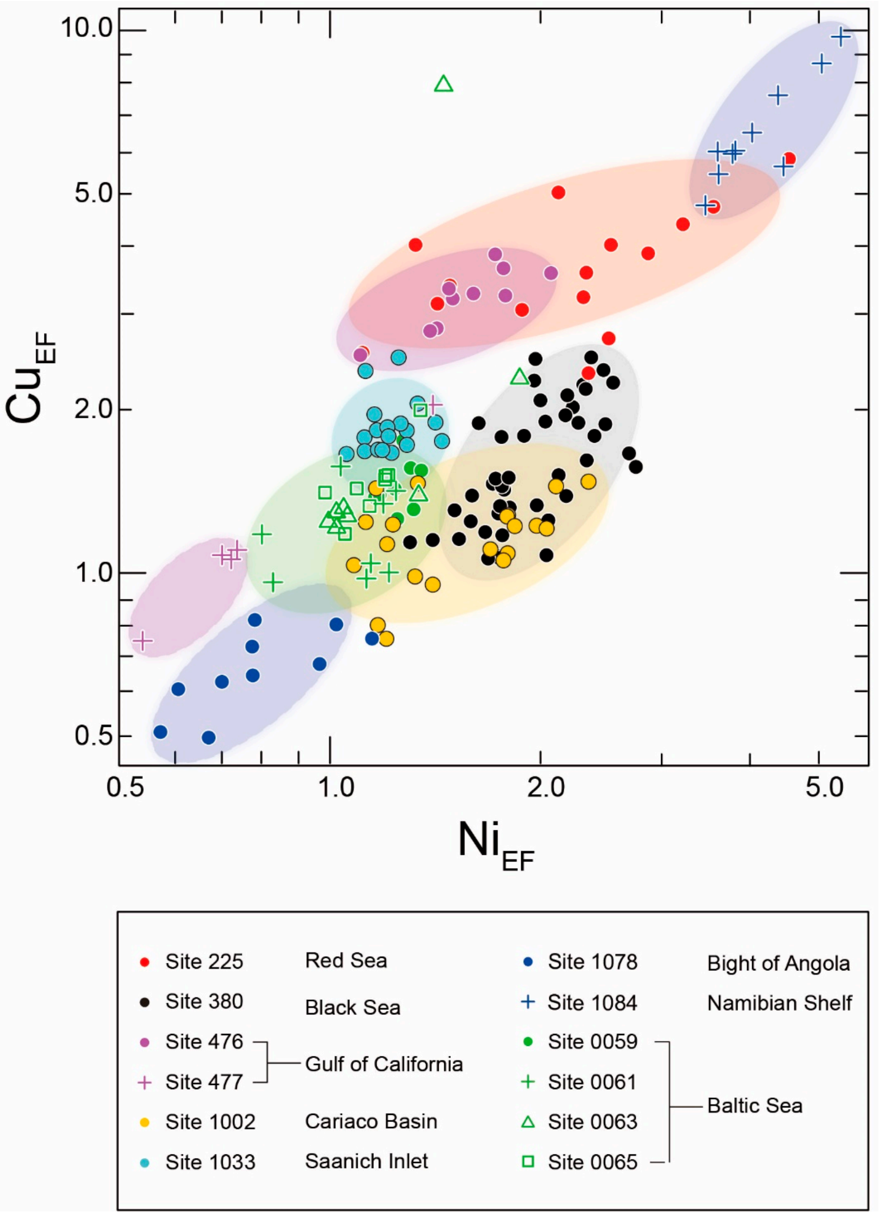

Figure 5. Scatter-diagram of enrichment factors for Ni (Ni_{EF}) versus Cu (Cu_{EF}). The shaded ellipses represent the data clusters corresponding to each site. The green ellipse represents all four sites in the Baltic Sea.

3.4. Variation of Enrichment Factors for Mo–U (Mo_{EF}–U_{EF}) and Geographical Conditions

In comparing enrichment factors for Mo and U (Mo_{EF} and U_{EF}, Figure 6a), sediments of the Cariaco Basin are mainly scattered within the "particulate shuttle" domain as reported by Algeo and Tribovillard [42], although the drilling sites are different. The particulate shuttle is a process in which particulate Fe-Mn-oxyhydroxides adsorb specific elements (e.g., Mo) above the redox boundary in the water column (i.e., chemocline), transport these elements as they settle, and release the elements as they dissolve below the chemocline or near the seafloor [42,67,68]. Owing to this efficient elemental transport process, redox-sensitive elements such as Mo adsorbed on Fe-Mn particles can be concentrated in the sediment of sea areas where the surface water mass is connected to the open ocean and a chemocline develops in the water column. Our samples from the Cariaco Basin capture the signature of this process.

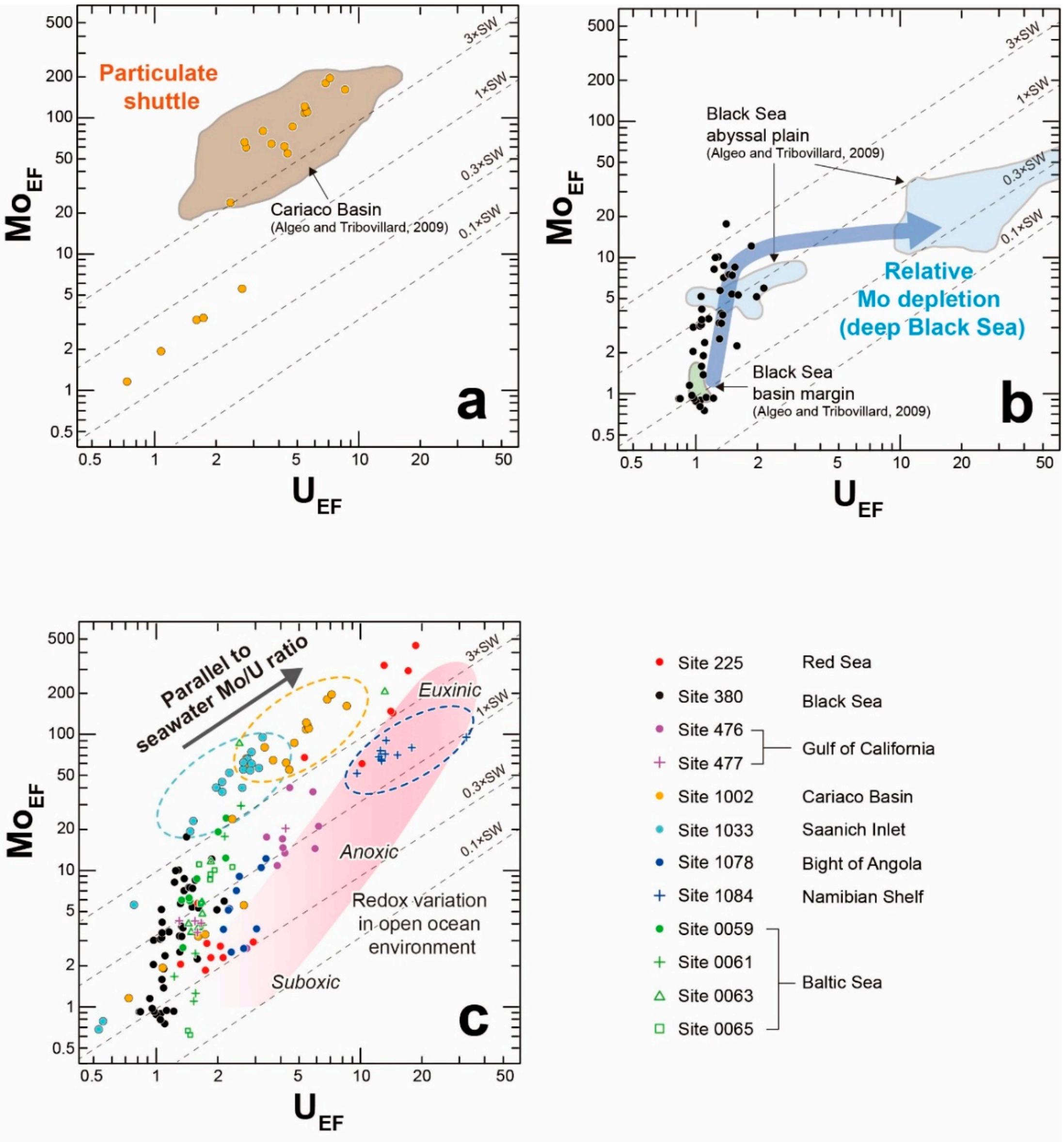

Figure 6. Scatter-diagrams of enrichment factors for U (U_{EF}) versus Mo (Mo_{EF}). Dashed lines denote 0.1, 0.3, 1 and 3 times the Mo:U weight-ratio in modern seawater [42,69]. (**a**) Data for the Cariaco Basin sediments in this study. Brown area shows the “particulate shuttle” domain reported by Algeo and Tribovillard [42]. (**b**) Data for the Black Sea sediments in this study. Green and light-blue domains show the data distribution corresponding to basin-margin and abyssal-plain sediments, respectively, in the Black Sea [42]. The dark-blue arrow represents the trend of relative depletion of Mo to U inferred from the sediments in the deep Black Sea. (**c**) All data from this study. The pink band represents the inferred pathway of redox variation [69]. Dashed ellipses represent the data clusters corresponding to each site.

According to Algeo and Tribovillard [42], Mo_{EF} and U_{EF} in Black Sea sediments (Figure 6b) show “evolution of water-mass chemistry” or a decreasing trend of the aqueous Mo:U ratio from surface water to deep water below the chemocline. In contrast to the Cariaco Basin, the depletion of Mo from seawater below the chemocline results in the lower Mo:U ratios of the Black Sea sediments compared to that of normal seawater (blue arrow in Figure 6b). The Black Sea samples in this study were collected from near the Bosporus Strait on the basin apron at a water depth of 2107 m (Figure 1), within the deep-basin setting [45]. However, in the Mo_{EF}–U_{EF} diagram (Figure 6b), they are plotted around the domains of the basin-margin and abyssal-plain sediments of the Black Sea (the green domain and the leftmost of the blue domains in Figure 6b, respectively), showing relatively low authigenic enrichment of Mo and U (generally Mo_{EF} <10 and U_{EF} <2). These sediments do not show the higher authigenic enrichment of these elements (Mo_{EF} >10 and U_{EF} >10) reported by Algeo and Tribovillard [42] (rightmost of the blue domains in Figure 6b). Our Black Sea samples (Site 380 Unit V) were interpreted as having been deposited under a brackish–marine environment, on the basis of microfossil assemblages [45]. Therefore, the absence of sediments clearly recording any evolution of water-mass chemistry (i.e., samples enriched in authigenic Mo and U with low Mo:U ratios) could be attributed to 1) a composition of seawater different from the modern one, and/or 2) a water depth shallower than the chemocline at the time of deposition of this lithological unit. Considering that palynological analyses suggested the age near the bottom of Unit V as the late Miocene [45], the possible change in sea level and/or the depth of the chemocline might be related to the Messinian Salinity Crisis (MSC; [70–72]), although a recent age model suggests that the deposition of Site 380 Unit V preceded the MSC [73].

A plot of Mo_{EF} vs. U_{EF} for all samples in this study (Figure 6c) shows an overall positive correlation. Most samples have an Mo_{EF} of 1–200, whereas a few samples from the Red Sea have values over 200. For U_{EF}, most samples range from 1 to 20. The Mo:U values for our samples range from a low of about 0.3 times the Mo:U ratio of modern seawater (plotted on the dashed line labeled "0.3 × SW" in Figure 6) to a high of more than 3 times the ratio of modern seawater (the domain above the dashed line "3 × SW" in Figure 6), with increasing enrichment factors of both Mo and U. Mo and U start to concentrate at different redox potentials. Uptake of authigenic U by marine sediments begins at the Fe(II)–Fe(III) redox boundary that corresponds to suboxic conditions [74]. This process occurs under less anoxic conditions than the formation of authigenic Mo that requires the presence of hydrogen sulfide (H_2S) in the water column (i.e., euxinic conditions) [3,75,76]. This difference in solubility due to redox conditions might result in variations of sediment Mo:U ratios—low Mo:U ratios under suboxic conditions and high Mo:U ratios under more anoxic condition [42]. In this context, if samples with high Mo_{EF} reflect a shift of seawater redox condition to more anoxic or euxinic condition, the samples should be scattered across the lines of seawater Mo:U ratios. However, the samples showing relatively high Mo_{EF} values ($Mo_{EF} > 20$ in Figure 6c; the major portion of Saanich Inlet (Site 1033), Cariaco Basin (Site 1002), and Namibian Shelf (Site 1084)) are scattered parallel to the trend denoting the seawater Mo:U ratio (i.e., dashed lines of 3 × SW or 1 × SW in Figure 6). This suggests that the Mo:U ratios of these sediments are relatively constant and thus the redox condition does not change significantly at these sites. In other words, the concomitant increase of Mo_{EF} and U_{EF} in these high Mo_{EF} sediments is not simply attributable to a shift of seawater redox conditions and it is necessary to consider factors other than changes in the redox condition to increase Mo_{EF} and U_{EF}.

The samples from each sea area constitute clusters in the Mo_{EF} vs. U_{EF} diagram (Figure 6c) as well as in the Ni_{EF} vs. Cu_{EF} diagram (Figure 5). This feature is also evident in a boxplot showing the data for each sea area (Figure 7). The Red Sea samples are divided into two groups, and thus the boxes covering the 1st to 3rd quantiles are wider than those for the other areas. One group of Red Sea samples that are enriched in authigenic Mo and U minerals corresponds to the Fe-enriched samples that deviate from the major trends for the relationships between Al_2O_3 and Fe_2O_3 and between CaO and Fe_2O_3 (Section 3.1), whereas the others have low authigenic Mo and U due to dilution with detrital components and carbonate.

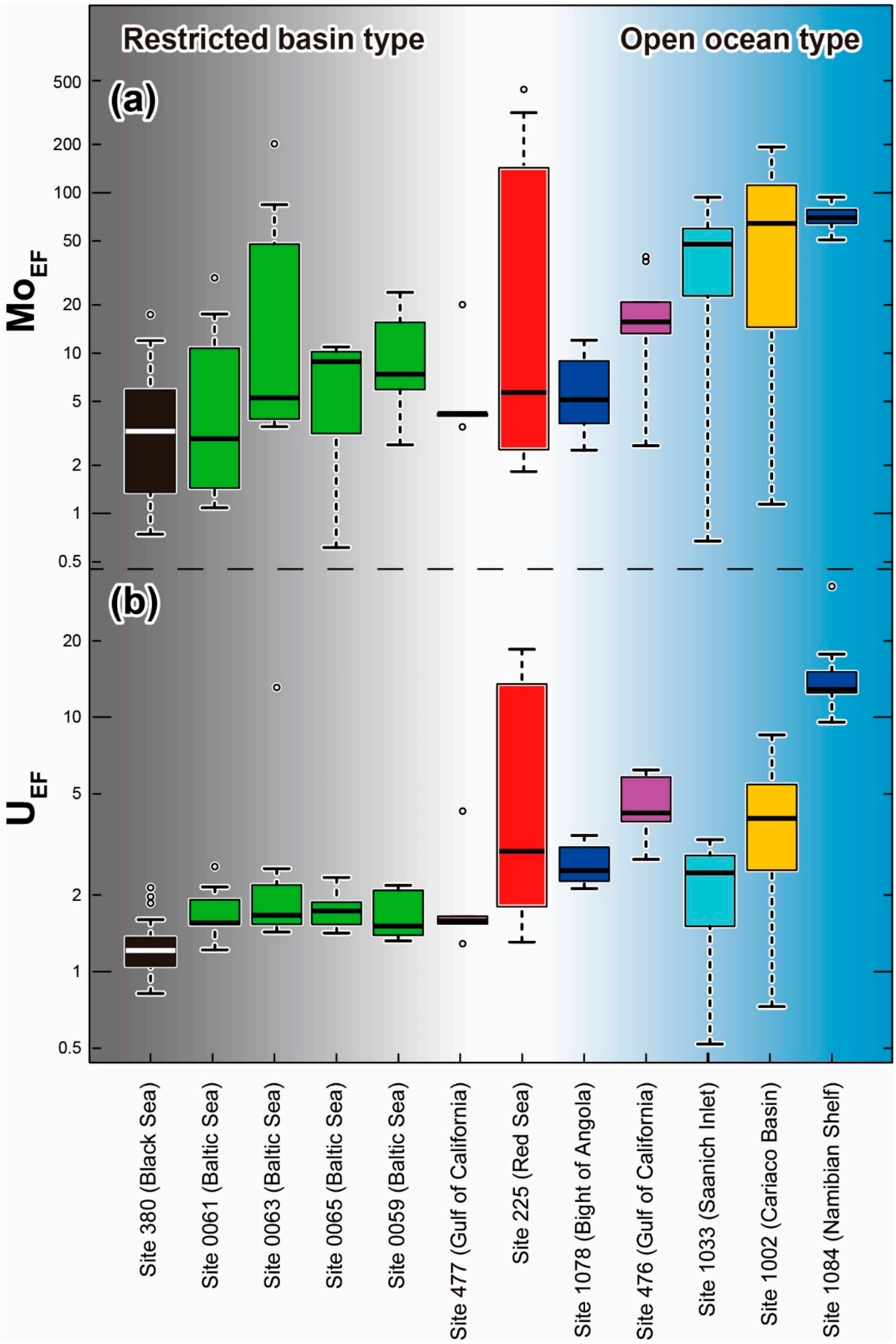

Figure 7. Box-plots of (**a**) Mo_{EF} and (**b**) U_{EF} for each sea area. The thick black line (white for Site 380) in each box denotes the median. The top and bottom of each box correspond to the 3rd quantile ($Q_{3/4}$) and 1st quantile ($Q_{1/4}$), respectively. The whiskers extend to the most extreme data point which is no more than 1.5 times the interquartile range (IQR) from the box, corresponding to an interval $[Q_{1/4} - 1.5 \times IQR, Q_{3/4} + 1.5 \times IQR]$ where $IQR = Q_{3/4} - Q_{1/4}$. Hollow circles are outlier samples deviating from this interval.

Focusing on all characteristics of the data clusters, the sea areas with higher Mo and U enrichment generally correspond to regions influenced by open-ocean water masses, whereas the areas with lower Mo and U enrichment are more restricted marine environments (Figures 1 and 7). Both Mo and U are elements abundant in seawater compared with other redox-sensitive and sulfide-forming trace elements, despite their low contents in the upper continental crust [58]. Algeo and Lyons [41] suggested that sedimentary Mo concentrations are controlled mainly by the degree of water-mass restriction in modern anoxic silled basins. This is because the dissolved Mo in the deep water-mass becomes depleted as the degree of restriction increases. Considering the positive correlations between Mo_{EF} and U_{EF} (Figure 6c) and the geographical trend in Mo and U enrichment in the sediment (Figure 7), U has properties similar to Mo under oxygen-depleted conditions. This is consistent with previous works on modern estuarine sediments [77] and organic-rich shales from the modern to Precambrian [78], both of which indicate that U concentrations in the sediments reflect dissolved U concentrations in oxygen-depleted water. Therefore, significant Mo and U enrichment could be attributed to the contribution of open-ocean seawater. In such a system, after the removal of Mo and U from the water column through precipitation under oxygen-depleted conditions, these elements could be replenished from adjacent open-ocean areas, thus maintaining high concentrations in the sediments. As mentioned above, the Mo_{EF}–U_{EF} diagram suggests that the particulate shuttle contributes to elemental precipitation in the Cariaco Basin [42] and probably in Saanich Inlet (Figure 6a,c). The particulate shuttle works in stratified water columns with oxic surface and anoxic deep water layers [42,67,68], which is consistent with the supply of oxic open-ocean water. Hence, the degree of Mo and U enrichment may reflect geographical conditions in terms of proximity to the open ocean.

4. Conclusions

We examined the bulk geochemistry of modern sediments from eight oxygen-depleted environments. The samples are considered to be a mixture of terrigenous detrital materials and biogenic carbonate on the basis of their contents of major elements. Some redox-sensitive and sulfide-forming elements in these sediments might be controlled by organic matter content (e.g., U), whereas others could be contained as sulfide minerals (e.g., As). The strikingly sharp linear relationship between Ni_{EF} and Cu_{EF} may reflect the similarity of their geochemical behaviors under oxygen-depleted conditions. Ni_{EF} and Cu_{EF} coincidently showed their highest values at the Namibian Shelf site, which is characterized by high primary productivity. The covariation of Mo_{EF} and U_{EF}, and difference in values of Mo_{EF} and U_{EF} among sea areas suggest that the degree of Mo and U enrichment may reflect geographical conditions in terms of proximity to the open ocean, or the degree of the supply of these elements from the open ocean. Our results suggest that paleoenvironmental and paleoceanographic reconstruction based on the concentration of redox sensitive elements requires comprehensive consideration of the chemical composition and redox potential of seawater, as well as paleogeographical conditions.

Supplementary Materials: The following are available online at http://www.mdpi.com/2075-163X/10/11/1021/s1, Figure S1: Scatter-diagrams for all pairs of enrichment factors for V, Cr, Co, Ni, Cu, Zn, As, Mo and U, Table S1: Major, trace and rare-earth elements, total organic carbon and total sulfur data for all the sediment samples analyzed in this study.

Author Contributions: Conceptualization, M.Y., K.Y. and Y.K.; methodology, M.Y, K.Y., K.N. and M.I.; investigation, M.Y., K.Y. and M.I.; resources, M.Y., K.Y. and Y.K.; data curation, M.Y.; writing—original draft preparation, M.Y.; writing—review and editing, all authors; visualization, M.Y. and K.Y.; supervision, Y.K.; funding acquisition, Y.K, K.N. and K.Y. All authors have read and agreed to the published version of the manuscript.

Funding: This research was financially supported by Japan Society for the Promotion of Science (JSPS) KAKENHI Grants No. 15H05771 to Y.K., No. 17H01361 to N.K. and No. 20H02678 to K.Y.

Acknowledgments: The samples used in this study were provided by the International Ocean Discovery Program (IODP). This study was performed under the cooperative research program of the Center for Advanced Marine Core Research (CMCR), Kochi University (Accept nos 17B068, 18A015, 18B014, 19A0014, 19B012). We thank

Y. Itabashi, C. Kabashima and the staff at the CMCR for their assistance with chemical analyses. We also thank two anonymous reviewers for their constructive comments.

Conflicts of Interest: The authors declare no conflict of interest.

References

1. Vine, J.D.; Tourtelot, E.B. Geochemistry of black shale deposits—A summary report. *Econ. Geol.* **1970**, *65*, 253–272. [CrossRef]
2. Calvert, S.E.; Pedersen, T.F. Geochemistry of Recent oxic and anoxic marine sediments: Implications for the geological record. *Mar. Geol.* **1993**, *113*, 67–88. [CrossRef]
3. Crusius, J.; Calve, S.; Pedersen, T.; Sage, D. Rhenium and molybdenum enrichments in sediments as indicators of oxic, suboxic and sulfidic conditions of deposition. *Earth Planet. Sci. Lett.* **1996**, *145*, 65–78. [CrossRef]
4. Algeo, T.J.; Maynard, J.B. Trace-element behavior and redox facies in core shales of Upper Pennsylvanian Kansas-type cyclothems. *Chem. Geol.* **2004**, *206*, 289–318. [CrossRef]
5. Tribovillard, N.; Algeo, T.J.; Lyons, T.; Riboulleau, A. Trace metals as paleoredox and paleoproductivity proxies: An update. *Chem. Geol.* **2006**, *232*, 12–32. [CrossRef]
6. Rimmer, S.M. Geochemical paleoredox indicators in Devonian—Mississippian black shales, Central Appalachian Basin (USA). *Chem. Geol.* **2004**, *206*, 373–391. [CrossRef]
7. Ocubalidet, S.G.; Rimmer, S.M.; Conder, J.A. Redox conditions associated with organic carbon accumulation in the Late Devonian New Albany Shale, west-central Kentucky, Illinois Basin. *Int. J. Coal Geol.* **2018**, *190*, 42–55. [CrossRef]
8. Algeo, T.J. Can marine anoxic events draw down the trace element inventory of seawater? *Geology* **2004**, *32*, 1057–1060. [CrossRef]
9. Xiang, L.; Zhang, H.; Schoepfer, S.D.; Cao, C.-Q.; Zheng, Q.-F.; Yuan, D.-X.; Cai, Y.-F.; Shen, S.-Z. Oceanic redox evolution around the end-Permian mass extinction at Meishan, South China. *Palaeogeogr. Palaeoclimatol. Palaeoecol.* **2020**, *544*, 109626. [CrossRef]
10. Grasby, S.E.; Beauchamp, B.; Embry, A.; Sanei, H. Recurrent Early Triassic ocean anoxia. *Geology* **2013**, *41*, 175–178. [CrossRef]
11. Kato, Y.; Nakao, K.; Isozaki, Y. Geochemistry of Late Permian to Early Triassic pelagic cherts from southwest Japan: Implications for an oceanic redox change. *Chem. Geol.* **2002**, *182*, 15–34. [CrossRef]
12. Takahashi, S.; Yamasaki, S.; Ogawa, Y.; Kimura, K.; Kaiho, K.; Yoshida, T.; Tsuchiya, N. Bioessential element-depleted ocean following the euxinic maximum of the end-Permian mass extinction. *Earth Planet. Sci. Lett.* **2014**, *393*, 94–104. [CrossRef]
13. Takahashi, S.; Nakada, R.; Watanabe, Y.; Takahashi, Y. Iron-depleted pelagic water at the end-Permian mass extinction inferred from chemical species of iron and molybdenum in deep-sea sedimentary rocks. *Palaeogeogr. Palaeoclimatol. Palaeoecol.* **2019**, *516*, 384–399. [CrossRef]
14. Algeo, T.J.; Kuwahara, K.; Sano, H.; Bates, S.; Lyons, T.; Elswick, E.; Hinnov, L.; Ellwood, B.; Moser, J.; Maynard, J.B. Spatial variation in sediment fluxes, redox conditions, and productivity in the Permian–Triassic Panthalassic Ocean. *Palaeogeogr. Palaeoclimatol. Palaeoecol.* **2011**, *308*, 65–83. [CrossRef]
15. Brennecka, G.A.; Herrmann, A.D.; Algeo, T.J.; Anbar, A.D. Rapid expansion of oceanic anoxia immediately before the end-Permian mass extinction. *Proc. Natl. Acad. Sci. USA* **2011**, *108*, 17631–17634. [CrossRef]
16. Westermann, S.; Stein, M.; Matera, V.; Fiet, N.; Fleitmann, D.; Adatte, T.; Föllmi, K.B. Rapid changes in the redox conditions of the western Tethys Ocean during the early Aptian oceanic anoxic event. *Geochimica Cosmochimica Acta* **2013**, *121*, 467–486. [CrossRef]
17. Hetzel, A.; Böttcher, M.E.; Wortmann, U.G.; Brumsack, H. Paleo-redox conditions during OAE 2 reflected in Demerara Rise sediment geochemistry (ODP Leg 207). *Palaeogeogr. Palaeoclimatol. Palaeoecol.* **2009**, *273*, 302–328. [CrossRef]
18. Broecker, W.S.; Peng, T.H. *Tracers in the Sea*; Eldigio Press: New York, NY, USA, 1982; pp. 28–40.
19. Kato, Y.; Fujinaga, K.; Nakamura, K.; Takaya, Y.; Kitamura, K.; Ohta, J.; Toda, R.; Nakashima, T.; Iwamori, H. Deep-sea mud in the Pacific Ocean as a potential resource for rare-earth elements. *Nat. Geosci.* **2011**, *4*, 535–539. [CrossRef]
20. Yasukawa, K.; Liu, H.; Fujinaga, K.; Machida, S.; Haraguchi, S.; Ishii, T.; Nakamura, K.; Kato, Y. Geochemistry and mineralogy of REY-rich mud in the eastern Indian Ocean. *J. Asian Earth Sci.* **2014**, *93*, 25–36. [CrossRef]

21. Yasukawa, K.; Nakamura, K.; Fujinaga, K.; Machida, S.; Ohta, J.; Takaya, Y.; Kato, Y. Rare-earth, major, and trace element geochemistry of deep-sea sediments in the Indian Ocean: Implications for the potential distribution of REY-rich mud in the Indian Ocean. *Geochem. J.* **2015**, *49*, 621–635. [CrossRef]
22. Yasukawa, K.; Nakamura, K.; Fujinaga, K.; Iwamori, H.; Kato, Y. Tracking the spatiotemporal variations of statistically independent components involving enrichment of rare-earth elements in deep-sea sediments. *Sci. Rep.* **2016**, *6*, 29603. [CrossRef] [PubMed]
23. Machida, S.; Fujinaga, K.; Ishii, T.; Nakamura, K.; Hirano, N.; Kato, Y. Geology and geochemistry of ferromanganese nodules in the Japanese Exclusive Economic Zone around Minamitorishima Island. *Geochem. J.* **2016**, *50*, 539–555. [CrossRef]
24. Nozaki, T.; Tokumaru, A.; Takaya, Y.; Kato, Y.; Suzuki, K.; Urabe, T. Major and trace element compositions and resource potential of ferromanganese crust at Takuyo Daigo Seamount, northwestern Pacific Ocean. *Geochem. J.* **2016**, *50*, 527–537. [CrossRef]
25. Azami, K.; Hirano, N.; Machida, S.; Yasukawa, K.; Kato, Y. Rare earth elements and yttrium (REY) variability with water depth in hydrogenetic ferromanganese crusts. *Chem. Geol.* **2018**, *493*, 224–233. [CrossRef]
26. Jenkyns, H.C. Geochemistry of oceanic anoxic events. *Geochem. Geophys. Geosyst.* **2010**, *11*, Q03004. [CrossRef]
27. Iijima, K.; Yasukawa, K.; Fujinaga, K.; Nakamura, K.; Machida, S.; Takaya, Y.; Ohta, J.; Haraguchi, S.; Nishio, Y.; Usui, Y.; et al. Discovery of extremely REY-rich mud in the western North Pacific Ocean. *Geochem. J.* **2016**, *50*, 557–573. [CrossRef]
28. Fujinaga, K.; Yasukawa, K.; Nakamura, K.; Machida, S.; Takaya, Y.; Ohta, J.; Araki, S.; Liu, H.; Usami, R.; Maki, R.; et al. Geochemistry of REY-rich mud in the Japanese Exclusive Economic Zone around Minamitorishima Island. *Geochem. J.* **2016**, *50*, 575–590. [CrossRef]
29. Takaya, Y.; Yasukawa, K.; Kawasaki, T.; Fujinaga, K.; Ohta, J.; Usui, Y.; Nakamura, K.; Kimura, J.-I.; Chang, Q.; Hamada, M.; et al. The tremendous potential of deep-sea mud as a source of rare-earth elements. *Sci. Rep.* **2018**, *8*, 5763. [CrossRef]
30. Yasukawa, K.; Ohta, J.; Mimura, K.; Tanaka, E.; Takaya, Y.; Usui, Y.; Fujinaga, K.; Machida, S.; Nozaki, T.; Iijima, K.; et al. A new and prospective resource for scandium: Evidence from the geochemistry of deep-sea sediment in the western North Pacific Ocean. *Ore Geol. Rev.* **2018**, *102*, 260–267. [CrossRef]
31. Mimura, K.; Nakamura, K.; Yasukawa, K.; Machida, S.; Ohta, J.; Fujinaga, K.; Kato, Y. Significant impacts of pelagic clay on average chemical composition of subducting sediments: New insights from discovery of extremely rare-earth elements and yttrium-rich mud at Ocean Drilling Program Site 1149 in the western North Pacific Ocean. *J. Asian Earth Sci.* **2019**, *186*, 104059. [CrossRef]
32. Ohta, J.; Yasukawa, K.; Machida, S.; Fujinaga, K.; Nakamura, K.; Takaya, Y.; Iijima, K.; Suzuki, K.; Kato, Y. Geological factors responsible for REY-rich mud in the western North Pacific Ocean: Implications from mineralogy and grain size distributions. *Geochem. J.* **2016**, *50*, 591–603. [CrossRef]
33. Ohta, J.; Yasukawa, K.; Nozaki, T.; Takaya, Y.; Mimura, K.; Fujinaga, K.; Nakamura, K.; Usui, Y.; Kimura, J.-I.; Chang, Q.; et al. Fish proliferation and rare-earth deposition by topographically induced upwelling at the late Eocene cooling event. *Sci. Rep.* **2020**, *10*, 9896. [CrossRef]
34. Nakamura, K.; Machida, S.; Okino, K.; Masaki, Y.; Iijima, K.; Suzuki, K.; Kato, Y. Acoustic characterization of pelagic sediments using sub-bottom profiler data: Implications for the distribution of REY-rich mud in the Minamitorishima EEZ, western Pacific. *Geochem. J.* **2016**, *50*, 605–619. [CrossRef]
35. Yasukawa, K.; Ohta, J.; Miyazaki, T.; Vaglarov, B.S.; Chang, Q.; Ueki, K.; Toyama, C.; Kimura, J.-I.; Tanaka, E.; Nakamura, K.; et al. Statistic and isotopic characterization of deep-sea sediments in the western North Pacific Ocean: Implications for genesis of the sediment extremely enriched in rare-earth elements. *Geochem. Geophys. Geosyst.* **2019**, *20*, 3402–3430. [CrossRef]
36. Tanaka, E.; Nakamura, K.; Yasukawa, K.; Mimura, K.; Fujinaga, K.; Iijima, K.; Nozaki, T.; Kato, Y. Chemostratigraphy of deep-sea sediments in the western North Pacific Ocean: Implications for genesis of mud highly enriched in rare-earth elements and yttrium. *Ore Geol. Rev.* **2020**, *119*, 103392. [CrossRef]
37. Hirst, D.M. Geochemistry of Sediments from Eleven Black Sea Cores. In *Black Sea-Geology, Chemistry, and Biology*; Degens, E.T., Ross, D.A., Eds.; American Association of Petroleum Geologists: Tulsa, OK, USA, 1974; Volume 20, pp. 330–355.

38. Piper, D.Z.; Dean, W.E.; US Geological Survey. *Trace-element Deposition in the Cariaco Basin, Venezuela Shelf, under Sulfate-reducing Conditions—A History of the Local Hydrography and Global Climate, 20 Ka to the Present*; Professional Paper; US Geological Survey: Reston, VA, USA, 2002; pp. 1–41. [CrossRef]
39. François, R. A study on the regulation of the concentrations of some trace metals (Rb, Sr, Zn, Pb, Cu, V, Cr, Ni, Mn and Mo) in Saanich Inlet sediments, British Columbia Canada. *Mar. Geol.* **1988**, *83*, 285–308. [CrossRef]
40. Skei, J. Geochemical and sedimentological considerations of a permanently anoxic fjord-Framvaren, south Norway. *Sediment. Geol.* **1983**, *36*, 131–145. [CrossRef]
41. Algeo, T.J.; Lyons, T.W. Mo—Total organic carbon covariation in modern anoxic marine environments: Implications for analysis of paleoredox and paleohydrographic conditions. *Palaeoceanography* **2006**, *21*, PA1016. [CrossRef]
42. Algeo, T.J.; Tribovillard, N. Environmental analysis of paleoceanographic systems based on molybdenum–uranium covariation. *Chem. Geol.* **2009**, *268*, 211–225. [CrossRef]
43. Sweere, T.; van den Boorn, S.; Dickson, A.J.; Reichart, G.-J. Definition of new trace-metal proxies for the controls on organic matter enrichment in marine sediments based on Mn, Co, Mo and Cd concentrations. *Chem. Geol.* **2016**, *441*, 235–245. [CrossRef]
44. Whitmarsh, R.B.; Ross, D.A.; Ali, S.; Boudreaux, J.E.; Coleman, R.; Fleisher, R.L.; Girdler, R.W.; Manheim, F.T.; Matter, A.; Nigrini, C.; et al. *Initial Reports DSDP*; US Government Printing Office: Washington, DC, USA, 1974; Volume 23.
45. Ross, D.A.; Neprochnov, Y.; Degens, E.T.; Erickson, A.J.; Hunt, J.M.; Manheim, F.; Percival, S.; Senalp, M.; Stoffers, P.; Supko, P.; et al. *Initial Reports DSDP*; US Government Printing Office: Washington, DC, USA, 1978; Volume 42.
46. Curray, J.R.; Moore, D.G.; Eduardo Aguayo, J.; Aubry, M.-P.; Einsele, G.; Fornari, D.; Gieskes, J.; Guerrero-Garcia, J.; Kastner, M.; Kelts, K.; et al. *Initial Reports DSDP*; US Government Printing Office: Washington, DC, USA, 1982; Volume 64.
47. Sigurdsson, H.; Leckie, R.M.; Acton, G.D.; Abrams, L.J.; Bralower, T.J.; Carey, S.N.; Chaisson, W.P.; Cotillon, P.; Cunningham, A.D.; D'Hondt, S.L.; et al. *Proc. Ocean Drilling Program, Initial Reports*; Ocean Drilling Program: College Station, TX, USA, 1997; p. 165.
48. Bornhold, B.D.; Firth, J.V.; Adamson, L.M.; Baldauf, J.G.; Blais, A.P.; Elvert, M.; Fox, P.J.; Hebda, R.; Kemp, A.E.S.; Moran, K.; et al. *Proc. Ocean Drilling Program, Initial Reports*; Ocean Drilling Program: College Station, TX, USA, 1998; p. 169S.
49. Wefer, G.; Berger, W.H.; Richter, C.; Adams, D.D.; Anderson, L.D.; Andreasen, D.J.; Brüchert, V.; Cambray, H.; Christensen, B.A.; Frost, G.M.; et al. *Proc. Ocean Drilling Program, Initial Reports*; Ocean Drilling Program: College Station, TX, USA, 1998; p. 175.
50. Andrén, T.; Jørgensen, B.B.; Cotterill, C.; Green, S.; Andrén, E.; Ash, J.; Bauersachs, T.; Cragg, B.; Fanget, A.-S.; Fehr, A.; et al. *Scientists, Proc. IODP*; Andrén, T., Jørgensen, B.B., Cotterill, C., Green, S., The Expedition 347, Eds.; Integrated Ocean Drilling Program: College Station, TX, USA, 2015; p. 347.
51. Kato, Y.; Ohta, I.; Tsunematsu, T.; Watanabe, Y.; Isozaki, Y.; Maruyama, S.; Imai, N. Rare earth element variations in mid-Archean banded iron formations: Implications for the chemistry of ocean and continent and plate tectonics. *Geochim. Cosmochim. Acta* **1998**, *62*, 3475–3497. [CrossRef]
52. Kato, Y.; Fujinaga, K.; Suzuki, K. Major and trace element geochemistry and Os isotopic composition of metalliferous umbers from the Late Cretaceous Japanese accretionary complex. *Geochem. Geophys. Geosyst.* **2005**, *6*, Q07004. [CrossRef]
53. Irino, T. Quantification of Kosa (Eolian Dust) Contribution to the Sediments and Reconstruction of Its Flux Variation at ODP Site 797, the Japan Sea during the Last 200 Kyr. Ph.D. Thesis, University Tokyo, Tokyo, Japan, 1996.
54. Aries, S.; Valladon, M.; Polvé, M.; Dupré, B. A routine method for oxide and hydroxide interference corrections in ICP-MS chemical analysis of environmental and geological samples. *Geostand. Newslett.* **2000**, *24*, 19–31. [CrossRef]
55. Makishima, A.; Nakamura, E. Determination of major/minor and trace elements in silicate samples by ICP-QMS and ICP-SFMS applying isotope dilution-internal standardization (ID-IS) and multi-stage internal standardisation. *Geostand. Geoanal. Res.* **2006**, *30*, 245–271. [CrossRef]

56. Takaya, Y.; Hiraide, T.; Fujinaga, K.; Nakamura, K.; Kato, Y. A study on the recovery method of rare-earth elements from REY-rich mud toward the development and the utilization of REY-rich mud. *J. MMIJ* **2014**, *130*, 104–114. (In Japanese with English abstract). [CrossRef]
57. Larson, T.E.; Heikoop, J.M.; Perkins, G.; Chipera, S.J.; Hess, M.A. Pretreatment technique for siderite removal for organic carbon isotope and C:N ratio analysis in geological samples. *Rapid Commun. Mass Spectrom.* **2008**, *22*, 865–872. [CrossRef]
58. Rudnick, R.L.; Gao, S. Composition of the Continental Crust. In *Treatise on Geochemistry*, 2nd ed.; Holland, H.D., Turekian, K.K., Eds.; Elsevier Ltd.: Amsterdam, The Netherlands, 2014; pp. 1–51. [CrossRef]
59. Lindh, A.; Lindh, A. Chemical composition of Late Svecofennian granite in the Bothnian Basin, central Sweden. *GFF* **2014**, *136*, 483–502. [CrossRef]
60. Martinez, N.C.; Murray, R.W.; Thunell, R.C.; Peterson, L.C.; Lorenzoni, L.; Astor, Y.; Varela, R. Local and regional geochemical signatures of surface sediments from the Cariaco Basin and Orinoco Delta, Venezuela. *Geology* **2010**, 159–162. [CrossRef]
61. Gromet, L.P.; Dymek, R.F.; Haskin, L.A.; Korotev, R.L. The "North American shale composite": Its compilation, major and trace element characteristics. *Geochim. Cosmochim. Acta* **1984**, *48*, 2469–2482. [CrossRef]
62. Garzanti, E.; Andò, S.; Vezzoli, G.; Lustrino, M.; Boni, M.; Vermeesch, P. Petrology of the Namib Sand Sea: Long-distance transport and compositional variability in the wind-displaced Orange Delta. *Earth Sci. Rev.* **2012**, *112*, 173–189. [CrossRef]
63. Huerta-Diaz, M.A.; Morse, J.W. Pyritization of trace metals in anoxic marine sediments. *Geochim. Cosmochim. Acta* **1992**, *56*, 2681–2702. [CrossRef]
64. Morse, J.W.; Luther, G.W. Chemical influences on trace metal-sulfide interactions in anoxic sediments. *Geochim. Cosmochim. Acta* **1999**, *63*, 3373–3378. [CrossRef]
65. Soua, M. Productivity and bottom water redox conditions at the Cenomanian–Turonian Oceanic Anoxic Event in the Southern Tethyan Margin, Tunisia. *Revue Méditerranéenne l'Environnement* **2010**, *4*, 653–664.
66. Hay, W.W.; Brock, J.C. Temporal variation in intensity of upwelling off southwest Africa. *Geol. Soc. Spec. Publ.* **1992**, *64*, 463–497. [CrossRef]
67. Trefry, J.H.; Presley, B.J.; Keeney-Kennicutt, W.L.; Trocine, R.P. Distribution and chemistry of manganese, iron, and suspended particulates in Orca Basin. *Geo-Mar. Lett.* **1984**, *4*, 125–130. [CrossRef]
68. Ho, T.-Y.; Taylor, G.T.; Astor, Y.; Varela, R.; Müller-Karger, F.; Scranton, M.I. Vertical and temporal variability of redox zonation in the water column of the Cariaco Basin: Implications for organic carbon oxidation pathways. *Mar. Chem.* **2004**, *86*, 89–104. [CrossRef]
69. Tribovillard, N.; Algeo, T.J.; Baudin, F.; Riboulleau, A. Analysis of marine environmental conditions based on molybdenum–uranium covariation—Applications to Mesozoic paleoceanography. *Chem. Geol.* **2012**, *324*, 46–58. [CrossRef]
70. Hsü, K.J.; Ryan, W.B.F.; Cita, M.B. Late Miocene desiccation of the Mediterranean. *Nature* **1973**, *242*, 240–244. [CrossRef]
71. Hsü, K.J.; Montadert, L.; Bernoulli, D.; Cita, M.B.; Erickson, A.; Garrison, R.E.; Kidd, R.B.; Mèlierés, F.; Müller, C.; Wright, R. History of the Mediterranean salinity crisis. *Nature* **1977**, *267*, 399–403. [CrossRef]
72. Ryan, W.B.F. Decoding the Mediterranean salinity crisis. *Sedimentology* **2009**, *56*, 95–136. [CrossRef]
73. Van Baak, C.G.C.; Vasiliev, I.; Palcu, D.V.; Dekkers, M.J. A Greigite-based magnetostratigraphic time frame for the Late Miocene to Recent DSDP Leg 42B Cores from the Black Sea. *Front. Earth Sci.* **2016**, *4*, 1–18. [CrossRef]
74. Zheng, Y.; Anderson, R.F.; Van Geen, A.; Fleisher, M.Q. Remobilization of authigenic uranium in marine sediments by bioturbation. *Geochim. Cosmochim. Acta* **2002**, *66*, 1759–1772. [CrossRef]
75. Helz, G.R.; Miller, C.V.; Charnock, J.M.; Mosselmans, J.F.W.; Pattrick, R.A.D.; Garner, C.D.; Vaughan, D.J. Mechanism of molybdenum removal from the sea and its concentration in black shales: EXAFS evidence. *Geochim. Cosmochim. Acta* **1996**, *60*, 3631–3642. [CrossRef]
76. Zheng, Y.; Anderson, R.F.; van Geen, A.; Kuwabara, J. Authigenic molybdenum formation in marine sediments: A link to pore water sulfide in the Santa Barbara Basin. *Geochim. Cosmochim. Acta* **2000**, *64*, 4165–4178. [CrossRef]

77. Barnes, C.E.; Cochran, J.K. Uranium geochemistry in estuarine sediments: Controls on removal and release processes. *Geochim. Cosmochim. Acta* **1993**, *57*, 555–569. [CrossRef]
78. Partin, C.A.; Bekker, A.; Planavsky, N.J.; Scott, C.T.; Gill, B.C.; Li, C.; Podkovyrov, V.; Maslov, A.; Konhauser, K.O.; Lalonde, S.V.; et al. Large-scale fluctuations in Precambrian atmospheric and oceanic oxygen levels from the record of U in shales. *Earth Planet. Sci. Lett.* **2013**, *369–370*, 284–293. [CrossRef]